

การศึกษาและประดิษฐ์โครงสร้างนาโนของอินเดียมฟอสไฟด์
ด้วยวิธีครอปเลทอพิแทกซ์จากล้าโมเลกุล



นางสาววิภากร จีวะสุวรรณ

วิทยานิพนธ์นี้เป็นส่วนหนึ่งของการศึกษาตามหลักสูตรปริญญาวิศวกรรมศาสตรดุษฎีบัณฑิต
สาขาวิชาวิศวกรรมไฟฟ้า ภาควิชาวิศวกรรมไฟฟ้า
คณะวิศวกรรมศาสตร์ จุฬาลงกรณ์มหาวิทยาลัย
ปีการศึกษา 2552
ลิขสิทธิ์ของจุฬาลงกรณ์มหาวิทยาลัย

**STUDY AND FABRICATION OF InP NANOSTRUCTURES
GROWN BY DROPLET MOLECULAR BEAM EPITAXY**

Miss Wipakorn Jevasuwan

**A Dissertation Submitted in Partial Fulfillment of the Requirements
for the Degree of Doctor of Philosophy Program in Electrical Engineering**

Department of Electrical Engineering

Faculty of Engineering

Chulalongkorn University

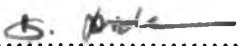
Academic year 2009

Copyright of Chulalongkorn University


522379

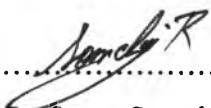
Thesis Title STUDY AND FABRICATION OF InP NANOSTRUCTURES
 GROWN BY DROPLET MOLECULAR BEAM EPITAXY
By Miss Wipakorn Jevasuwan
Field of Study Electrical Engineering
Thesis Advisor Associate Professor Somchai Ratanathamphan, D.Eng.
Thesis Co-advisor Professor Somsak Panyakeow, D.Eng.

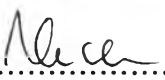
Accepted by the Faculty of Engineering, Chulalongkorn University in
Partial Fulfillment of the Requirements for the Doctoral Degree


.....  Dean of the Faculty of Engineering
(Associate Professor Boonsom Lerdhirunwong, Dr. Ing.)

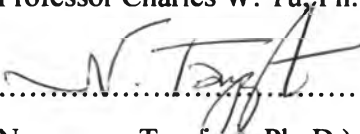
THESIS COMMITTEE


.....  Chairman
(Professor Virulh Sa-yakanit, Ph. D.)

.....  Thesis Advisor
(Associate Professor Somchai Ratanathamphan, D. Eng.)

.....  Thesis Co-advisor
(Professor Somsak Panyakeow, D. Eng.)

.....  External Examiner
(Professor Charles W. Tu, Ph. D.)

.....  External Examiner
(Noppawan Tanpipat, Ph. D.)

.....  External Examiner
(Associate Professor Satoshi Iwamoto, Ph. D.)

.....  External Examiner
(Assistant Professor Tanakorn Osothchan, Ph. D.)

วิทยากร จีวะสุวรรณ : การศึกษาและประดิษฐ์โครงสร้างนาโนของอินเดียมฟอสไฟด์ด้วยวิธีครอปเลทอิพิแทกซ์จากลำโมเลกุล. (STUDY AND FABRICATION OF InP NANOSTRUCTURES GROWN BY DROPLET MOLECULAR BEAM EPITAXY) อ. ที่ปรึกษาวิทยานิพนธ์หลัก : รศ. ดร. สมชัยรัตนธรรมพันธ์, อ. ที่ปรึกษาวิทยานิพนธ์ร่วม : ศ.ดร. สมศักดิ์ ปัญญาแก้ว, 113 หน้า.

การประดิษฐ์ควอนตัมดอทโมเลกุลรูปร่างแหวนของอินเดียมฟอสไฟด์ที่ก่อตัวขึ้นเอง ถูกนำเสนอขึ้นเป็นครั้งแรกในวิทยานิพนธ์นี้ อิทธิพลของตัวแปรในการปลูกผลึกที่มีต่อการก่อตัวและคุณสมบัติของควอนตัมดอทโมเลกุลรูปร่างแหวนของอินเดียมฟอสไฟด์ได้มีการศึกษาอย่างละเอียด ตัวอย่างควอนตัมดอทโมเลกุลรูปร่างแหวนของอินเดียมฟอสไฟด์ในเมตริกซ์ของอินเดียมแกลเลียมฟอสไฟด์ที่มีส่วนผสมของอินเดียมเท่ากับ 0.5 บนแผ่นฐานแกลเลียมอาร์เซไนต์ชนิดไม่มีการโด๊ป และมีระนาบ 001 ถูกเตรียมขึ้นด้วยเครื่องปลูกผลึกด้วยลำโมเลกุลที่มีชนิดสารตั้งต้นเป็นของแข็งและใช้เทคนิคการปลูกครอปเลทอิพิแทกซ์ ตัวแปรที่ทำการศึกษาร่วมกันโดยตรงกับกระบวนการสร้างอินเดียมครอปเลท และกระบวนการทำอินเดียมครอปเลทให้เป็นผลึกอินเดียมฟอสไฟด์ ซึ่งได้แก่ อุณหภูมิการสร้างอินเดียมครอปเลท, อุณหภูมิการทำให้เป็นผลึก, อัตราการสร้างอินเดียมครอปเลท และปริมาณอินเดียม คุณสมบัติของควอนตัมดอทโมเลกุลถูกทำการติดตามผลอย่างละเอียดระหว่างกระบวนการปลูกผลึก และภายหลังเสร็จสิ้นกระบวนการปลูกผลึก โดยการสังเกตรูปแบบการเลี้ยวเบนของการสะท้อนอิเล็กตรอนพลังงานสูง (Reflection High Energy Electron Diffraction), การวัดด้วยแรงอะตอม (Atomic Force Microscopy), การวัดด้วยกล้องจุลทรรศน์อิเล็กตรอนแบบส่องผ่าน (Transmission Electron Microscopy) และ การวัดโฟโตลูมิเนสเซนซ์ (Photoluminescence Spectroscopy)

จากผลการทดลองแสดงให้เห็นว่า การก่อตัวของควอนตัมดอทโมเลกุลรูปร่างแหวนของอินเดียมฟอสไฟด์เกิดขึ้นเนื่องจากความสามารถของเทคนิคครอปเลทอิพิแทกซ์ และค่าคงตัวผลึกที่แตกต่างกัน 3.8 เปอร์เซ็นต์ของอินเดียมฟอสไฟด์และอินเดียมแกลเลียมฟอสไฟด์ที่มีส่วนผสมของอินเดียมเท่ากับ 0.5 ความสม่ำเสมอของขนาดควอนตัมดอทที่ดีที่สุด และจำนวนสูงสุดของควอนตัมดอทโมเลกุลเท่ากับ 46 เปอร์เซ็นต์ ที่ประกอบด้วยเปดควอนตัมดอทต่อโมเลกุล สัมฤทธิ์ผลได้โดยการใช้ อุณหภูมิการสร้างอินเดียมครอปเลท, อุณหภูมิการทำให้เป็นผลึก, อัตราการสร้างอินเดียมครอปเลท และ ปริมาณอินเดียมเท่ากับ 250 °C, 200 °C, 1.6 ML/s และ 3.2 ML ตามลำดับ ค่ายอดและค่าความกว้างของสเปกตรัมโฟโตลูมิเนสเซนซ์ของควอนตัมดอทโมเลกุลรูปทรงวงแหวนของอินเดียมฟอสไฟด์ที่ได้จากเงื่อนไขการปลูกนี้มีค่าเท่ากับ 1.68 eV และ 43 meV ที่ 20 K และ 1.61 eV และ 60 meV ที่อุณหภูมิห้อง

ควอนตัมดอทโมเลกุลรูปทรงวงแหวนของอินเดียมฟอสไฟด์ที่สร้างขึ้นโดยเทคนิคครอปเลทอิพิแทกซ์ถูกทำการศึกษา และแสดงให้เห็นความเป็นไปได้ที่จะเป็นทางเลือกหนึ่ง ในการนำไปใช้กับเทคโนโลยีควอนตัมคอมพิวเตอร์ ความสำเร็จที่ได้จากการทดลองประดิษฐ์ควอนตัมดอทโมเลกุลรูปทรงวงแหวนของอินเดียมฟอสไฟด์ในวิทยานิพนธ์ฉบับนี้ นับเป็นจุดเริ่มต้นที่น่าสนใจในฐานะระบบสารที่ให้โครงสร้างควอนตัมดอทโมเลกุลรูปทรงวงแหวน ซึ่งจะเป็นตัวหลักสำคัญในการพัฒนาโครงสร้างดังกล่าวต่อไปในอนาคต

ภาควิชา วิศวกรรมไฟฟ้า
สาขาวิชา วิศวกรรมไฟฟ้า
ปีการศึกษา 2552

ลายมือชื่อนิสิต วิทยากร จีวะสุวรรณ
ลายมือชื่อ. ที่ปรึกษาวิทยานิพนธ์หลัก
ลายมือชื่อ. ที่ปรึกษาวิทยานิพนธ์ร่วม

4871875321 : MAJOR ELECTRICAL ENGINEERING

KEYWORDS: InP / InGaP / GaAs / NANOSTRUCTURES / MOLECULAR BEAM EPITAXY / DROPLET EPITAXY

WIPAKORN JEVASUWAN : STUDY AND FABRICATION OF InP NANOSTRUCTURES GROWN BY DROPLET MOLECULAR BEAM EPITAXY. THESIS ADVISOR : ASSOC. PROF. SOMCHAI RATANATHAMMAPHAN, D. Eng., THESIS CO-ADVISOR : PROF. SOMSAK PANYAKEOW, D. Eng., 113 pp.

The fabrication of self-assembled InP ring-shaped QDMs has been first proposed in this thesis. The influences of growth parameters on the formation and characteristics of InP ring-shaped QDMs have been intensively studied. The InP ring-shaped QDMs samples were prepared using solid-source MBE via droplet epitaxy technique in $\text{In}_{0.5}\text{Ga}_{0.5}\text{P}$ matrices on semi-insulating GaAs (001) substrate. The investigated parameters relating to the In droplet deposition and crystallization process were deposition temperature, crystallization temperature, In deposition rate and In amount. The InP ring-shaped QDMs properties were thoroughly evaluated by both *in situ* and *ex situ* monitoring including Reflection High Energy Electron Diffraction (RHEED), Atomic Force Microscopy (AFM), Transmission Electron Microscopy (TEM), and Photoluminescence Spectroscopy (PL).

The experimental results have shown that the formation of InP ring-shaped quantum dot molecules (QDMs) is owing to the performance of droplet epitaxy technique and the lattice mismatched between InP and $\text{In}_{0.5}\text{Ga}_{0.5}\text{P}$ of 3.8%. The best QD size homogeneity and the highest number of QDMs (46%) which consist of eight QDs per QDM was achieved with the deposition temperature, crystallization temperatures, In deposition rate and In coverage of 250 °C, 200 °C, 1.6 ML/s and 3.2 ML, respectively. The PL peaks and FWHMs of these InP ring-shaped QDMs are 1.68 eV and 43 meV at 20 K and 1.61 eV and 60 meV at room temperature.

InP ring-shaped QDMs grown by droplet epitaxy technique has been investigated and shows the feasibility as an alternative material system for quantum computing technologies. The achievement on this thesis should renew the interest of InP ring-shaped QDMs as a promising system and also be an important mile stone in the development of ring-shaped QDM structure.

Department: ... Electrical Engineering ...

Field of study: ... Electrical Engineering ..

Academic year: 2009

Student's signature *wipakorn jerasuwān*

Advisor's signature *Somchai Ratanathamphan*

Co-advisor's signature *Somsak Panyakeow*

ACKNOWLEDGEMENTS

The success of this thesis has been attributed to the extensive support and assistance from my advisor, Assoc. Prof. Dr. Somchai Ratanathamphan, and my co-advisor, Prof. Dr. Somsak Panyakeow. I am grateful for valuable advice and guidance in this research, for kindness in examining the research instrument, providing suggestions for improvement and offering many good opportunities.

I deeply thank to other lecturers and staffs of the Semiconductor Device Research Laboratory (SDRL), Assoc. Prof. Dr. Montri Sawadsaringkarn, Assoc. Prof. Dr. Banyong Toprasertpong, Assoc. Prof. Dr. Choopol Antarasena, Assoc. Prof. Dr. Songpol Kanjanachuchai, Dr. Chanin Wissawinthanon, Mrs. Bunditha Ratwiset, Mr. Supachock Thainoi, Mr. Pornchai Changmoang, Mr. Pattana Phuntuwong and Mrs. Kwanruan Thainoi, for their valuable advice, cheerfulness and kind support and thanks also go to my seniors, friends and juniors in the SDRL family especially Mr. Poonyasiri Boonpeng and Mr. Hassanet Sodabanlu for their help, encouragement and very kind assistance.

I would like to thank Dr. Noppadon Nuntawong and Ms. Puenisara Limnonthakul at National Electronics and Computer Technology Center (NECTEC) for their help and kindness advising for transmission electron microscopy that used in this research.

I wish to make deep acknowledgement to members of the thesis committee, Prof. Dr. Virulh Sa-yakanit, Prof. Dr. Charles W. Tu, Dr. Noppawan Tanpipat, Assoc. Prof. Dr. Satoshi Iwamoto, and Assist. Prof. Dr. Tanakorn Osothchan for their advice and helpful suggestion.

I would like to express my appreciation to Chulalongkorn University.

I would like to thank Toshiba Corporation that gave me a scholarship and a great opportunity for good experience in Japan.

I would like to give special thanks to the Royal Golden Jubilee (RGJ) scholarship for the research fund and financial support.

Finally, I am grateful to my family for their support, entirely care and love. The usefulness of this thesis, I dedicate to my father, my mother, all the teachers and all benefactors who have taught me since my childhood.

CONTENTS

	Page
Abstract (Thai)	iv
Abstract (English)	v
Acknowledgements	vi
Contents	vii
List of Tables	x
List of Figures	xi
List of Symbols	xxi
Chapter I Introduction	1
1.1 Historical Background and Motivation	1
1.2 Objective	4
1.4 Significant Benefits of the Research	4
1.5 Synopses	5
Chapter II Theories and Principles	6
2.1 Basic Concepts of Low-Dimensional Nanostructures	6
2.2 Strain Effect on Low-Dimensional Nanostructures	10
2.3 Growth of Self-Assembled Quantum Dots	15
2.3.1 Molecular Beam Epitaxy Growth Modes	15
2.3.2 Self-Assembled Growth in Stranski Krastanow Growth Mode	17
2.3.3 Thermodynamic and Kinetic theories of Self-Assembled Quantum Dot Formation in Equilibrium System	18
2.3.3.1 Thermodynamically Limited Growth	18
2.3.3.2 Kinetically Controlled Growth	22
2.3.4 Self-Assembled Growth by Droplet Epitaxy Technique	24
2.3.5 Thermodynamic and Kinetic Theories of Self-Assembled Ring-Shaped Nanostructures in Non-Equilibrium System ..	26

CONTENTS (continued)

		Page
2.4	Quantum Information Processing	30
	2.4.1 Quantum Cellular Automata	31
	2.4.2 Extended Quantum Cellular Automata	33
2.5	Material Considerations	35
Chapter III	Experimental Details	38
3.1	Molecular Beam Epitaxy	38
	3.1.1 Solid-Source Molecular Beam Epitaxy System Overview	39
3.2	Reflection High Energy Electron Diffraction	41
	3.2.1 RHEED Pattern Observation and Calibration	43
3.3	Scanning Electron Microscopy	47
3.4	High Resolution X-ray Diffractometer	48
3.5	Atomic Force Microscopy	50
3.6	Transmission Electron Microscopy	52
3.7	Photoluminescence Spectroscopy	53
3.8	Sample Preparation	56
Chapter IV	Experimental Results and Discussions	59
4.1	Characterization of In _{0.5} Ga _{0.5} P layer on GaAs Substrate	59
4.2	Monitoring of the InP ring-shaped Quantum Dot Molecule Formation by <i>in situ</i> RHEED Pattern	63
4.3	Possible Formation Mechanism of InP Ring-shaped Quantum Dot Molecules	64
4.4	Effect of Deposition Temperature on the Properties of InP Ring-shaped Quantum Dot Molecules	65
4.5	Effect of Crystallization Temperature on the Properties of InP Ring-shaped Quantum Dot Molecules	72
4.6	Effect of Indium Deposition Rate on the Properties of InP Ring-shaped Quantum Dot Molecules	78

CONTENTS (continued)

	Page
4.7 Effect of Indium Thickness on the Properties of InP Ring-shaped Quantum Dot Molecules	83
4.8 Power Dependence Photoluminescence of InP Ring-shaped Quantum Dot Molecules	88
4.9 Temperature Dependence Photoluminescence of InP Ring-shaped Quantum Dot Molecules	90
4.10 Characterization of InP Ring-shaped Quantum Dot Molecules by Transmission Electron Microscopy	92
Chapter V Conclusions	94
References	97
Appendix	104
List of Publications	105
List of Presentations	108
Vitae	113

LIST OF TABLES

	Page
Table 2.1 Properties of InP, In _{0.5} Ga _{0.5} P and GaAs semiconductors at room temperature (300 K) (Jalali and Pearton, 1995).	37

LIST OF FIGURES

		Page
Figure 2.1	Schematic views and graphs of density of states (D.O.S.) in semiconductor structures of decreasing dimensionality: bulk (3D), quantum well (2D), quantum wire (1D), quantum dot (0D).	7
Figure 2.2	Size- and material-dependent emission spectra of several surfactants coated semiconductor nanocrystal QDs (NCQDs) in a variety of sizes. The blue spectral lines are emitted by CdSe NCQDs with diameters of 2.1, 2.4, 3.1, 3.6, and 4.6 nm (from right to left). The green series is emitted by InP NCQDs with diameters of 3.0, 3.5, and 4.6 nm. The red series is emitted by InAs NCQDs with diameters of 2.8, 3.6, 4.6, and 6.0 nm. Within each color the wavelength is fine tuned by controlling the size of the QDs. The inset shows schematically the dependence of the fluorescence energy on the size of the QDs. (Redrawn from Hitchman, 1993)	9
Figure 2.3	Schematic representation of (a) unstrained layer, (b) compressive strained layer, and (c) tensile strained layer. The closed circles represent atoms of the substrate material and the open circles are atoms of the deposited material. In (b) and (c) the lattice constant of the deposited material are different from the epitaxial layer. The arrows in (b) and (c) represent forces (stresses) exerted on the epitaxial layer.	10
Figure 2.4	(a) A schematic representation of the band structure of an unstrained direct-gap tetrahedral semiconductor. The light-hole (LH) and heavy-hole (HH) bands degenerate at the Brillouin zone center Γ and the spin-split-off (SO) band lies lower in energy. The lowest conduction band (CB) is separated by the band gap energy (E_g) from the valence bands. Note that the $k_{ }$ is perpendicular to the growth and strain direction. (b) Under biaxial compression. (c) Under biaxial tension. The lower panel shows the VB diagram of the quantum well	

LIST OF FIGURES (continued)

		Page
	structure in case of (a) unstrained, (b) compressive strained and (c) tensile strain. (Redrawn from O'Reilly, 1989)	14
Figure 2.5	Strain distribution for a pyramidal QD with a 45° facet angle in the (xz) plane through the pyramid top. Identical isotropic elastic constants and $\sigma = 1/3$ are taken throughout the structure. ε_{xx} , ε_{yy} , ε_{zz} , ε_{xz} are shown; due to symmetry in this plane, ε_{xy} , and ε_{yz} are zero. (Bimberg et al., 1999)	15
Figure 2.6	Schematic representation of the three crystal growth modes (a) Layer-by-layer or Frank-van der Merwe; (b) island or Volmer-Weber; (c) layer-plus-island or Stranski-Krastanow mode.	16
Figure 2.7	Schematic representations of island formation during epitaxial growth of a semiconductor material on top of another one with a smaller lattice constant in Stranski-Krastanow growth mode.	18
Figure 2.8	Energy of an array of 3D coherently strained islands per one atom versus island size L. The control parameter α depends on the contribution from the surface energy and the edge energy (Bimberg et al., 1999).	20
Figure 2.9	Equilibrium phase diagram of lattice-mismatched heteroepitaxial system as a function of the total amount of deposited material and lattice mismatch. The small panels on the top and the bottom illustrate the morphology of the surface in the six growth modes. The small empty triangles indicate the presence of stable islands, while the large shaded ones refer to ripened islands (Daruka and Barabási, 1997).	21
Figure 2.10	(a) Schematic representation of the local strain energy density in and around the QD. The energy barrier for the adatom's diffusion to the QD has a maximum at the edge of the QD (Seifert et al., 1996). (b) The variation of the surface strain ε_s	

LIST OF FIGURES (continued)

		Page
	along the system surface and a contour diagram showing strain ε_{xx} in the island (Chen and Washburn, 1996).	23
Figure 2.11	Schematic illustration of SK QDs formation process (a) initial stage of wetting layer formation (b) the wetting layer (c) 2D to 3D islands transition, (d) non-uniform 3D islands (e) self-regulation process and (f) misfit dislocation formation.	24
Figure 2.12	Two basic processes of droplet epitaxy technique: (a) deposition of the group III elements to create the initial droplets (b) crystallization with the group V flux to form the semiconductor nanostructures and (c) some possible forming of semiconductor nanostructures with different group V flux intensity. (Redrawn from Mano et al., 2000)	25
Figure 2.13	Schematic illustration of the kinetic process of group III droplet with group V ambience. The arrows denote the direction of surface diffusions of group V atoms (green points) and group III atoms (red points) (Redrawn from Lee and Yang, (2009).	27
Figure 2.14	Layout of the four-dot QCA cell with two electrons and the two distinct electron configurations corresponding to their maximum spatial separation, which can be labeled logic “0” and “1” (Bajec et al., 2006).	32
Figure 2.15	The binary wire; propagation of enforced logical values 0 and 1 along a line of QCA cells (Bajec et al., 2006).	32
Figure 2.16	The QCA majority gate: AND, OR, and NOT (Bajec et al., 2006). ...	32
Figure 2.17	Layout of the eight-dot EQCA cell with two electrons and the four distinct electron configurations corresponding to their maximum spatial separation, which can be labeled logic “0”, “1” and “1/2” (Bajec et al., 2006).	33
Figure 2.18	The ternary wire; propagation of enforced configuration ‘A’ or ‘B’ along a line of EQCA cells.	33

LIST OF FIGURES (continued)

		Page
Figure 2.19	The EQCA majority gate truth table, AND and OR (Bajec et al., 2006).	34
Figure 2.20	Lattice constant versus energy gap at room temperature for the III-Vs material system. The solid line is for direct band gap material and the dotted line is for indirect band gap material.	35
Figure 2.21	The zinc blende crystal structure.	36
Figure 3.1	The RIBER 32P SS-MBE machine at semiconductor devices research laboratory (SDRL), Chulalongkorn University.	40
Figure 3.2	A schematic drawing of the RIBER 32P SS-MBE growth chamber.	40
Figure 3.3	A schematic representation of the RHEED observation system.	42
Figure 3.4	(a) a schematic representation of the RHEED geometry (Herman and Sitter, 1989), (b) the imaging of RHEED pattern that is determined by the Laue method-intersection of Ewald sphere in reciprocal lattice space and (c) an example of Ewald sphere construction for a reconstructed surface in $[1\bar{1}0]$ azimuth and RHEED pattern of GaAs (001) 2×4 surface in $[1\bar{1}0]$ and $[110]$ azimuth (Ichimiya and Cohen, 2004).	42
Figure 3.5	(a) Schematic representation of top view, side view of relaxed structure (Esser et al., 2001) and $\alpha(4\times 4)$ RHEED pattern of GaAs surface at 460°C in $[1\bar{1}0]$ and $[100]$ azimuths; and (b) Schematic representation of top view, side view of relaxed structure (LaBella et al., 1999) and (2×4) RHEED pattern of GaAs surface at 580°C in $[1\bar{1}0]$ and $[110]$ azimuths. Filled and empty circles represent As and Ga, respectively. Larger circles represent atoms closer to the surface.	44
Figure 3.6	The RHEED pattern transition of temperature calibration process of GaAs in $[1\bar{1}0]$ azimuth ($T_{\text{transition}} (500^\circ\text{C}) =$	

LIST OF FIGURES (continued)

		Page
	$(T_1+T_2+T_3+T_4) / 4$	44
Figure 3.7	(a) Schematic representation of the interpretation of RHEED intensity oscillations and (b) are experimental results obtained during the growth of GaAs. The intensity signals were detected in the pattern area marked by white boxes shown in the insets (Shchukin and Bimberg, 1999).	45
Figure 3.8	Figure 3.8 Plots of growth rates of GaAs (a) and InAs (b) as a function of BEP. The GaAs growth rates were calibrated by RHEED intensity oscillation while the InAs growth rate was obtained from RHEED pattern transition during the growth of self-assembled QDs. All RHEED data were obtained from a 2×2 cm ² GaAs substrate glued in the middle of a molybdenum block under As-rich condition.	46
Figure 3.9	A JEOL JSM-5400 electron microscope at Analytical Instrument Center and Laboratory (AICL), Chulalongkorn University and schematic of SEM measurement.	48
Figure 3.10	Lattice planes and Bragg's law.	49
Figure 3.11	The PHILIPS X' Pert PRO diffractometer at Nakano-Sugiyama-Tanemura Laboratory, The University of Tokyo.	50
Figure 3.12	The SEIKO SPA 400-AFM at SDRL, Chulalongkorn University and a schematic of AFM measurement.	51
Figure 3.13	Modes of AFM measurement.	51
Figure 3.14	A JEOL JEM-2010 electron microscope at National Electronics and Computer Technology Center (NECTEC) and its schematic diagram.	52
Figure 3.15	The micro-PL system at Nakano-Sugiyama-Tanemura Laboratory, The University of Tokyo.	54
Figure 3.16	The macro-PL setup and its schematic at SDRL, Chulalongkorn University.	54

LIST OF FIGURES (continued)

		Page
Figure 3.17	Simple interpretation of the PL data obtained from a QD structure. In case of small QD (a): the PL peak energy position is higher compared with large QD (b).	55
Figure 3.18	Simple interpretation of the PL spectrum obtained from the QD structure. In (a) the PL spectrum is very narrow due to the delta-function like density of states; and in (b) the average dot size corresponds to the PL peak energy position and the PL linewidth corresponds to the size distribution of the array.	55
Figure 3.19	Schematic diagram of the sample structure grown in this work. The growth conditions for the InP ring-shaped QDMs layer were given in the text.	58
Figure 4.1	The SEM image of 1- μ m-thick InGaP layer grown on GaAs (001) substrate.	60
Figure 4.2	The XRD spectrum of 200 nm InGaP layer grown on GaAs (001) substrate in (004).	61
Figure 4.3	The room temperature (300 K) PL spectrum of 200-nm-thick InGaP layer grown on GaAs (001) substrate.	62
Figure 4.4	RHEED patterns of each experimental procedure in $[1\bar{1}0]$ azimuth and $[110]$ azimuth.	63
Figure 4.5	Schematic representations of the self-organized InP ring-shaped QDMs formation: (a) In droplet deposits on $\text{In}_{0.5}\text{Ga}_{0.5}\text{P}$ layer and creates the initial droplet with the InP thin layer. (b) during crystallization time, In migrates away from center to periphery of the droplet, P atoms diffuse into the droplet and the lattice mismatch between the InP and $\text{In}_{0.5}\text{Ga}_{0.5}\text{P}$ layer form the QDMs structure (c).	65
Figure 4.6	The 2D top-view and 3D tiled-view AFM images and cross-sectional line-profiles along $[1\bar{1}0]$ of InP ring-shaped QDMs formed at different deposition temperature of (a) 120°C (b) 150°C	

LIST OF FIGURES (continued)

		Page
	(c) 180°C (d) 210°C (e) 250°C and (f) 290°C and crystallization at 200°C. The 3.2-ML thick indium coverage was deposited at a of 0.8 ML/s.	66
Figure 4.7	The dependence of InP QDs and ring-shaped QDMs densities and average outer and inner diameters of InP ring-shaped QDMs on the deposition temperature.	67
Figure 4.8	Distributions of the number of InP QDs per InP ring-shaped QDM ((a-f)-1), height ((a-f)-2) and lateral size of InP QDs ((a-f)-3) with various deposition temperatures.	68
Figure 4.9	The dependence of the number of InP QDs per InP ring-shaped QDM, height and lateral size of InP QDs on the deposition temperature.	69
Figure 4.10	The 2D top-view AFM images of InP ring-shaped QDMs formed at deposition temperature of 250 °C, the crystallization temperature of 200 °C, the In deposition rate of 0.8 ML/s and the In deposition rate of 3.2 ML with different substrate temperature ramping of (a) 250°C (b) 300°C and (c) 350°C after crystallization.	71
Figure 4.11	PL spectra of InP ring-shaped QDMs with various deposition temperatures measured by the macro-PL system at 20 K.	71
Figure 4.12	PL spectra of InP ring-shaped QDMs with various deposition temperatures measured by the micro-PL system at room temperature.	72
Figure 4.13	The 2D top-view and 3D tiled-view AFM images and cross-sectional line- profiles along $[1\bar{1}0]$ of InP ring-shaped QDMs formed at different crystallization temperature of (a) 150°C (b) 200°C (c) 250°C and (d) 300°C. The deposition temperature was 200°C with coverage of 3.2 ML indium droplet and indium deposition rate of 0.8 ML/s.	73

LIST OF FIGURES (continued)

		Page
Figure 4.14	The dependence of InP QDs and ring-shaped QDMs densities and average outer and inner diameters of InP ring-shaped QDMs on the crystallization temperature.	74
Figure 4.15	Distributions of the number of InP QDs per InP ring-shaped QDM ((a-d)-1), height ((a-d)-2) and lateral size of InP QDs ((a-d)-3) with various crystallization temperatures.	75
Figure 4.16	The dependence of the number of InP QDs per InP ring-shaped QDM, height and lateral size of InP QDs on the crystallization temperature.	76
Figure 4.17	PL spectra of InP ring-shaped QDMs with various crystallization temperatures measured by the macro-PL system at 20 K.	77
Figure 4.18	PL spectra of InP ring-shaped QDMs with various crystallization temperatures measured by the micro-PL system at room temperature.	77
Figure 4.19	The 2D top-view and 3D tiled-view AFM images and cross-sectional line- profiles along $[1\bar{1}0]$ of InP ring-shaped QDMs formed at different indium deposition rate of (a) 0.2 ML/s (b) 0.4 ML/s, (c) 0.8 ML/s and (d) 1.6 ML/s. The deposition and crystallization temperature was 250°C and 200°C, respectively with coverage of 3.2 ML indium droplet.	79
Figure 4.20	The dependence of InP QDs and ring-shaped QDMs densities and average outer and inner diameters of InP ring-shaped QDMs on the indium deposition rate.	80
Figure 4.21	Distributions of the number of InP QDs per InP ring-shaped QDM ((a-d)-1), height ((a-d)-2) and lateral size of InP QDs ((a-d)-3) with various indium deposition rate.	81
Figure 4.22	The dependence of the number of InP QDs per InP ring-shaped QDM, height and lateral size of InP QDs on the indium deposition rate.	82

LIST OF FIGURES (continued)

		Page
Figure 4.23	PL spectra of InP ring-shaped QDMs with various indium deposition rate measured by the macro-PL system at 20 K.	82
Figure 4.24	PL spectra of InP ring-shaped QDMs with various indium deposition rate measured by the micro-PL system at room temperature.	83
Figure 4.25	The 2D top-view and 3D tiled-view images and cross-sectional line-profiles along $[1\bar{1}0]$ of InP ring-shaped QDMs formed at different indium thickness of (a) 1.6 ML (b) 3.2 ML, (c) 4.8 ML and (d) 6.4 ML. The deposition and crystallization temperature were 250°C and 200°C, respectively with indium deposition rate of 0.8 ML/s.	84
Figure 4.26	The dependence of InP QRs, QDs and ring-shaped QDMs densities and average outer and inner diameters of InP QRs and ring-shaped QDMs on the indium thickness.	85
Figure 4.27	Distributions of the number of InP QDs per InP ring-shaped QDM ((b-d)-1), height ((a-d)-2) and lateral size of InP QRs and QDs ((a-d)-3) with various indium thickness.	86
Figure 4.28	The dependence of the number of InP QDs per InP ring-shaped QDM, height and lateral size of InP QRs and QDs on the indium thickness.	87
Figure 4.29	PL spectra of InP QRs and ring-shaped QDMs with various indium thickness measured by the macro-PL system at 20 K.	87
Figure 4.30	PL spectra of InP QRs and ring-shaped QDMs with various indium thickness measured by the micro-PL system at room temperature.	88
Figure 4.31	Power dependent PL spectra of InP ring-shaped QDMs which have the deposition temperature of 250 °C, the crystallization temperature of 200 °C, the In deposition rate of 1.6 ML/s and	

LIST OF FIGURES (continued)

		Page
	the In deposition rate of 3.2 ML.	89
Figure 4.32	The relationship between excitation powers, FWHMs and peak emission positions.	90
Figure 4.33	Temperature dependent PL spectra of InP ring-shaped QDMs which have the deposition temperature of 250 °C, the crystallization temperature of 200 °C, the In deposition rate of 1.6 ML/s and the In deposition rate of 3.2 ML.	91
Figure 4.34	The relationship between temperatures, FWHMs and peak emission positions.	91
Figure 4.35	(a) Schematic of sample structure for TEM measurement, (b) Overview cross-sectional TEM micrograph of InP ring-shaped QDM sample with the deposition temperature of 250 °C, the crystallization temperature of 200 °C, the indium deposition rate of 1.6 ML/s and the indium deposition rate of 3.2 ML and (c) Cross-sectional TEM micrograph of the upper InP ring-shaped QDMs layer.	93

LIST OF SYMBOLS

∇^2	Laplacian operator
α	control parameter
a_0	space between surface sites
$a_{//}$	parallel lattice constant
a_{\perp}	perpendicular lattice constant
a_e	lattice constant of deposited material
a_s	lattice constant of substrate material
A	surface area
AFM	atomic force microscopy
AICL	Analytical Instrument Center and Laboratory
Ar^+	argon
As	arsenic
AsBr_3	arsenic tribromide
AsH_3	arsine
BEP	beam equivalent pressure
C_0	concentration of group III atoms on the droplet boundary
C_{11}, C_{12}	elastic constant of epitaxial layer
CB	conduction band
CCD	charge-coupled device
CdSe	cadmium selenide
CEO	cleaved-edge overgrowth
CRT	cathode ray tube
0D	zero dimension
1D	one dimension
2D	two dimension
3D	three dimension
δ	delta function
Δh	height of nanostructure
Δt	short time or limit time
$\Delta\gamma$	change of surface free energy

LIST OF SYMBOLS (continued)

d_0	strained epitaxial film thickness
d_1	substrate thickness
$D_{0,III}$	prefactor
$D_{\text{bulk}}(E)$	bulk density of state
D_{III}	diffusion coefficient of group III atoms
$D_{\text{QW}}(E)$	quantum well density of state
$D_{\text{QWR}}(E)$	quantum wire density of state
$D_{\text{QD}}(E)$	quantum dot density of state
D.O.S.	density of state
ε	lattice mismatch or misfit strain
ε_{xx}	axial strain in x-direction
ε_{yy}	axial strain in y-direction
ε_{zz}	axial strain in z-direction
ε_{xz}	shear strain on x-plane directed through z-direction
ε_{xy}	shear strain on x-plane directed through y-direction
ε_{yz}	shear strain on y-plane directed through z-direction
$\varepsilon_{//}$	in-plane strain
ε_{\perp}	strain in perpendicular to the growth direction
E	carrier energy or total energy per unit cell
$E(L)$	total energy per unit volume
E_0	characteristic energy
E_a	adsorption energy and the
E_{bulk}	carrier energy of bulk
E_d	energy barrier for the hopping between surface sites
E_g	band gap energy
$E_{l,x}$	quantized energy in x-direction
$E_{m,y}$	quantized energy in y-direction
$E_{n,z}$	quantized energy in z-direction
E_{QW}	carrier energy of quantum well
E_{QWR}	carrier energy of quantum wire

LIST OF SYMBOLS (continued)

E_{QD}	carrier energy of quantum dot
E_{WL}	energy of wetting layer
E_{rip}	energy of ripened island
E_{island}	energy of single island
E_{elastic}	elastic strain energy
E_{st}	strain energy
E_{surface}	island surface energy
E_{edge}	island edge energy
EQCA	extended quantum dot cellular automata
$F(\mathbf{r})$	envelope wave function
FM	Frank van der Merwe
FWHM	full width at half maximum
γ_e	surface free energy of the epilayer/vacuum interface
γ_i	surface free energy of epilayer/substrate interface
γ_s	surface free energy of the substrate/vacuum interface
\mathbf{G}	reciprocal lattice vector
Ga	gallium
GaAs	gallium arsenide
GaP	gallium phosphide
GaSb	gallium antimony
Ge	germanium
GS-MBE	gas-source molecular beam epitaxy
h	Planck's constant or height of pyramidal quantum dot or final height
\hbar	reduced Planck's constant
h_0	thickness of monolayer
h_c	critical thickness of strained layer
HH	heavy-hole band
InAs	indium arsenide
InGaAs	indium gallium arsenide

LIST OF SYMBOLS (continued)

InGaP	indium gallium phosphide
InP	indium phosphide
k	Boltzmann constant or amplitude of wave vector
K	Knudsen
k_B	Boltzmann's constant
$k_{//}$	amplitude of in-plane (y-z) wave vector
k_{\perp}	amplitude of wave vector in x-direction
$\mathbf{k} = (k_x, k_y, k_z)$	carrier wave vector
k_{in}	wave vectors of incident electron
k_{diff}	wave vectors of diffraction electron
λ	elastic modulus or wavelength of the x-ray
$\lambda_{de\ Broglie}$	de Broglie wavelength
l	quantum number in x-direction
L	macroscopic length scale or base size of pyramidal quantum dot
L_0	characteristic length
LaB ₆	Lanthanum Hexaboride
L_{opt}	optimal island size
LH	light-hole band
LN ₂	liquid nitrogen
LPE	liquid phase epitaxy
m	quantum number in y-direction or mass of an group V atom
m_0	mass of an electron, 9.11×10^{-31} kg
m_e	effective electron mass
m_h	effective electron mass
m^*	carrier effective mass
MBE	molecular beam epitaxial or molecular beam epitaxy
ML	monolayer

LIST OF SYMBOLS (continued)

Mo	molybdenum
MOCVD	metalorganic chemical vapour deposition
MO-MBE	metal-organic molecular beam epitaxy
ν_{PR}	Poisson's ratio
n	quantum number in z-direction or an integer representing the order of the diffraction peak
N_A	Avogadro constant
N_D	volume density of quantum dot
$N_{(i)III-V}$	final shape of nanostructures
N_{III}	amount of diffused group III atoms
N_{III-V}	total amount per unit time
N_V	amount of the trapped group V atoms
N_{wi}	area density of the quantum wires
p	carrier momentum
P	intensity of group V flux
P_2	phosphorus dimers
P_4	phosphorous tetramers
PBN	pyrolytic boron nitride
PH_3	phosphine
PL	photoluminescence
Q	total deposited material (monolayer)
Q_1	deposited material that form wetting layer
Q_2	deposited material that form coherent 3D island
QCA	quantum dot cellular automata
QW	quantum well
QWR	quantum wire
QD	quantum dot
QDM	quantum dot molecule
QR	quantum ring
r_c	trapping radius of droplet
r_{GaAs}	growth rate of gallium arsenide

LIST OF SYMBOLS (continued)

r_{III}	atomic radius of group III atoms
r_{InAs}	growth rate of indium arsenide
r_{InGaAs}	growth rates of indium gallium arsenide
$\mathbf{r} = (x, y, z)$	carrier position vector
R	amount of impacting group V atoms on the substrate per unit time
Re	rhenium
RHEED	reflection high-electron energy diffraction
RT	room temperature
SDRL	semiconductor devices research laboratory
SEM	scanning electron microscopy
SK	Stranski Krastanow
SO	spin-split-off band
SS-MBE	solid-source molecular beam epitaxy
STM	scanning tunneling microscope
Θ	Heaviside's unit step function
θ	scattering angle
t	film thickness
t_m	time of crystallization process
T	temperature
T_1	first temperature
T_2	second temperature
T_3	third temperature
T_4	fourth temperature
T_{sub}	substrate temperature
$T_{\text{buffer growth}}$	buffer growth temperature
$T_{\text{transition}}$	transition temperature
TEGa	triethylgallium
TEM	transmission electron microscopy
Ti	titanium
TMIn	trimethylindium

LIST OF SYMBOLS (continued)

UHV	ultra-high vacuum
ν_1	thermal vibration frequencies for the upward direction
ν_0	thermal vibration frequencies for the lateral direction
V_{droplet}	volume of droplet
$V_{m,III}$	molar volume of droplet
$V(r)$	confinement potential
VPE	vapor phase epitaxy
VW	Volmer Weber
W	tungsten
WL	wetting layer
x_n	In composition